Tidal conversion by subcritical topography

N.J. Balmforth [*] G.R. Ierley [†] W.R. Young [‡]

March 22, 2002

Abstract

We give analytical estimates of the rate at which energy is extracted from the barotropic tide at topography and converted into internal gravity waves. The ocean is idealized as an inviscid, vertically unbounded fluid on the $f-$plane. The gravity waves are treated by linear theory and freely escape to $z = \infty$. We investigate several topographies: a sinusoidal ripple; a set of Gaussian bumps; and an ensemble of "random topographies". In the third case, topographic profiles are generated by randomly selecting the amplitudes of a Fourier superposition so that the power spectral density is similar to that of submarine topography. Our focus is the dependence of the conversion rate (watts per square meter of radiated power) on the amplitude of the topography, h_0, and on a nondimensional parameter ϵ_*, defined as the ratio of the slope of an internal tidal rays to the maximum slope of the topography. If $\epsilon_* \ll 1$ then the theory of Bell (1975) indicates that the conversion is proportional to h_0^2. Our results span the interval $0 \leq \epsilon_* < 1$ and show that the enhancement above Bell's prediction is a smoothly and modestly increasing function of ϵ_*: For $\epsilon_* \to 1$, the conversion of sinusoidal topography is 56% greater than Bell's $\epsilon_* \ll 1$ estimate, whilst the enhancement is only 14% greater for a Gaussian bump. With random topography, the enhancement at $\epsilon_* = 0.95$ is typically about 6% greater than Bell's formula. The $\epsilon_* \ll 1$ approximation is therefore quantitatively accurate over the range $0 < \epsilon_* < 1$, implying that the conversion is roughly proportional to h_0^2. As ϵ_* is increased, the radiated waves develop very small spatial scales which are not present in the underlying topography, and when ϵ_* approaches

[*]Department of Applied Mathematics, University of California at Santa Cruz, CA 95064. njb@ams.ucsc.edu

[†]Scripps Institution of Oceanography, University of California at San Diego, CA 92093-0225. grierley@ucsd.edu

[‡]Scripps Institution of Oceanography, University of California at San Diego, CA 92093-0213. wryoung@ucsd.edu

unity, the associated spatial gradients become so steep that overturns must occur even if the tidal amplitude is very weak. The solutions formally become singular at $\epsilon_* = 1$, in a breakdown of linear, inviscid theory.

1 Introduction

The role of the internal tide in mixing the abyssal ocean is currently a fashionable topic in oceanography (Munk and Wunsch 1998, Ledwell et al. 2000). For the purpose of understanding deep-ocean mixing the single most important issue is to estimate the rate at which energy is extracted from the barotropic tide and radiated into internal gravity waves at topographic features. The simplest analytical estimates of this "conversion" (e.g., Bell 1975(a, b); Khatiwala 2002; Llewellyn Smith & Young 2002), assume *inter alia* that the topography is "weak" in the sense that the bottom boundary condition can be applied approximately at a flat surface instead of the actual bumpy bottom. This weak-topography approximation is justified provided that the topographic slopes are much less than the slope of the internal tidal rays. In other words, the ratio of the maximum topographic slope to the ray slope, a nondimensional parameter ϵ_*, must be small. The weak-topography approximation is valid, and the problem is solved, if $\epsilon_* \ll 1$.

The weak-topography approximation quickly leads to compact formulas expressing the conversion in terms of the spectral characteristics of the topography, the properties of the barotropic tide, and the ocean stratification. One could more confidently and usefully apply these results if their bounds of validity were better delineated. And the approximation would be more powerful if we better knew the structure of the first corrections which account for nonzero ϵ_*. The goal of the present work is to evaluate such corrections.

Previous studies of the effects of large topographic slope include ray-tracing models (Rattray 1960, Baines 1973), and numerical computations (Holloway and Merrifield 1999; Khatiwala 2002; Li 2002). Unfortunately, ray tracing is complicated and difficult to adapt to general situations, whereas direct numerical approaches encounter problems due to the generation of what appear to be extremely fine spatial scales in the wavefield (*cf.* Baines' figures, and recent solutions obtained by Polzin, 2002). Here, we adopt a new approach to the tidal conversion problem, and expose directly how the wavefield develops small scales as ϵ_* increases, and even becomes singular as $\epsilon_* \to 1$.

In section 2 we formulate the finite-slope conversion problem in terms of

a streamfunction. We give several formulas which can be used to calculate conversion rates from the Fourier representation of the streamfunction. Section 3 is a detailed account of the conversions produced by tidal flow over a sinusoidal bottom. In section 4 we introduce a family of topographic profiles which can limit to a periodically-spaced sequence of Gaussian bumps. By moving these bumps further apart, while maintaining their width, we estimate the finite-slope conversion produced by a Gaussian ridge. In section 5 we treat "random topography"; profiles generated by randomly selecting the amplitudes of a Fourier superposition and engineered so that the power spectral density is similar to submarine topography. We also present a calculation of the average conversion produced by an ensemble of such topographies, correct to second order in ϵ. Section 6 is the conclusion and discussion.

2 Formulation

We idealize the ocean as a rotating, inviscid fluid layer in which the tide sloshes to-and-fro along the x-direction; z denotes the vertical. The barotropic tide is modelled as the periodically reversing, spatially uniform flow

$$\boldsymbol{U} = U_0 \hat{\boldsymbol{x}} \cos \omega_0 t \,. \tag{1}$$

Conversion to internal gravity waves occurs because this tide flows over a bumpy bottom; we denote the vertical amplitude of the bottom bumps by h_0. We suppose that the ocean has unlimited vertical extent and consequently we require that, as $z \to +\infty$, there is only upward radiation.

Because the topography is independent of y, so too is the disturbance created by tidal action. Linearization is justified provided that the tidal excursion, U_0/ω_0, is much less than the scale of the topography. This parameter restriction also ensures that terms such as $U_0 \cos(\omega_0 t)\nabla^2\psi_x$ can be neglected relative to $\nabla^2\psi_t$. Thus, the governing fluid equations for the induced velocity (u, v, w), pressure p and buoyancy b, are

$$u_t - f_0 v + p_x = 0 \,, \qquad v_t + f_0 u = 0 \,, \qquad w_t + p_z - b = 0 \,, \tag{2}$$

and

$$b_t + N^2 w = 0 \,, \qquad u_x + w_z = 0 \,. \tag{3}$$

In these equations f_0 is the Coriolis frequency, N is the constant buoyancy frequency and the density is written as $\rho = \rho_0(1 - g^{-1}N^2 z - g^{-1}b)$.

The velocity in the (x, z)-plane can be represented using a streamfunction $\psi(x, z, t)$: $(u, w) = (-\psi_z, \psi_x)$. The problem then reduces to solving the internal gravity wave equation,

$$\nabla^2 \psi_{tt} + f_0^2 \psi_{zz} + N^2 \psi_{xx} = 0\,, \tag{4}$$

where $\nabla^2 = \partial_x^2 + \partial_z^2$. The bottom boundary condition is that

$$\psi(x, h, t) = U_0 h(x) \cos(\omega_0 t)\,. \tag{5}$$

The condition in (5) ensures that the total streamfunction, $-U_0 z \cos(\omega_0 t) + \psi$, vanishes on $z = h(x)$.

We study model topographies which are periodic in x with wavelength Λ and wavenumber

$$k_0 \equiv \frac{2\pi}{\Lambda}\,. \tag{6}$$

The examples considered below are

$$h = h_0 \cos k_0 x \quad \text{and} \quad h = h_0 \exp[-2\gamma \sin^2(k_0 x/2)]\,, \tag{7}$$

where γ is a nondimensional parameter, and the "random topography" obtained by Fourier superposition.

Ray angles and nondimensional variables

One remarkable property of the internal tide is that the rays emitted from topography make a fixed angle with the horizontal. To express this ray angle in terms of the three fundamental frequencies in this problem we define

$$\mu \equiv \sqrt{\frac{N^2 - \omega_0^2}{\omega_0^2 - f_0^2}}\,. \tag{8}$$

μ^{-1} is then the slope of the internal gravity wave rays generated by the tide. In other words, the internal-tidal beams form angles $\pm \tan^{-1}(1/\mu)$ with the horizontal.

We say that the topography is "weak" if the topographic slopes are everywhere *much* less than μ^{-1}; the topography is "subcritical" if the slopes are less than μ^{-1}; the topography is supercritical if the topographic slope is somewhere steeper than μ^{-1}.

It is convenient to introduce nondimensional coordinates

$$X \equiv k_0 x\,, \quad Z \equiv \mu k_0 z\,. \tag{9}$$

In the (X, Z)-plane the tidal rays enclose angles of $\pm 45^\circ$ with the horizontal. We also represent the topography in the form $h = h_0 H(X)$ where H is a nondimensional profile function (e.g., in the sinusoidal case, $H(X) = \cos X$). With this notation the bottom is at $Z = \epsilon H(X)$, where

$$\epsilon \equiv h_0 k_0 \mu \,. \tag{10}$$

In the sinusoidal case, the parameter ϵ is the ratio of the maximum topographic slope, $h_0 k_0$, to the slope of a tidal beam μ^{-1}.

We consider the steady-state wave conversion by looking for time-periodic solutions with the tidal frequency: we introduce $\varphi = \varphi_r + \mathrm{i}\varphi_i$, where

$$\psi = U_0 h_0 \Re\left\{e^{-\mathrm{i}\omega_0 t}\varphi\right\} = U_0 h_0 \left(\varphi_r \cos\omega_0 t + \varphi_i \sin\omega_0 t\right) \,, \tag{11}$$

so that (4) becomes

$$\varphi_{XX} = \varphi_{ZZ} \,. \tag{12}$$

The lower boundary condition in (5) then becomes $\varphi(X, \epsilon H) = H$. The mathematical problem is completed by insisting that there is only upwards energy flux as $Z \to \infty$. This radiation condition ensures that φ has both a real and an imaginary part.

Our formulation takes no account of the ocean surface which would reflect the internal tide back down to the bottom: the model ocean is vertically unbounded and the gravity waves escape freely to $z = \infty$. Using the weak-topography approximation, Khatiwala (2002) and Llewellyn Smith and Young (2002) have shown that the effect of an upper boundary is to greatly reduce the conversions produced by topography whose horizontal scale exceeds that of the internal tide. Inclusion of this important process introduces another nondimensional parameter measuring the ocean depth into the problem, and the current theory is valid only when this quantity is relatively large.

A Fourier representation

Because the geometry is periodic in x, a Fourier series is a natural way of representing the solution of (12). Thus we can solve (12), and simultaneously impose the radiation condition at $z = +\infty$, by writing

$$\mathrm{e}^{-\mathrm{i}\omega_0 t}\varphi(X, Z) = \sum_{n=-\infty}^{\infty} \phi_n \mathrm{e}^{\mathrm{i}(nX - |n|Z) - \mathrm{i}\omega_0 t} \,. \tag{13}$$

The construction in (13) has downwards vertical phase propagation (and therefore upwards energy propagation) at both positive and negative n. We emphasize a crucial limitation of (13): because the energy flux is upwards *everywhere* (even in the valleys below the crests of the topography) we are limited to the case in which the topography is strictly subcritical. In other words, (13) is correct only if the slope of the topography is everywhere shallower than the slope of the tidal beams. Once the topography is supercritical there is downwards energy propagation below the topographic crests. (There are interesting analogies between this issue and Rayleigh's hypothesis in optics; see, for example, Keller 2000.)

To complete the solution, we determine the coefficients ϕ_n in (13) by applying the boundary condition $\varphi(X, \epsilon H) = H$:

$$H(X) = \sum_{n=-\infty}^{\infty} \phi_n \exp\left[\mathrm{i}nX - \mathrm{i}|n|\epsilon H(X)\right] . \tag{14}$$

This is essentially a big set of linear equations for $\{\phi_n\}$ (a numerical recipe for solving the system is given in Appendix A). We recover the weak-topography approximation by assuming that $\epsilon \ll 1$. In this case we can neglect the term $-|n|\epsilon H$ in the exponential on the right-hand side of (14) and (14) is then a standard Fourier series. We deduce that $H(X) = \varphi(X, 0)$ and we recover the results of Bell (1975a) immediately. Our main goal here is to solve (14) over the entire subcritical range for several model topographies and so make an assessment of the accuracy of this weak-topography approximation.

The limitation to the subcritical case is restrictive (e.g., island arcs are supercritcal). However at mid-ocean ridges the large-scale Fourier components of the topography have subcritical slopes, while the small-scale components are supercritical. The transition occurs at topography with a horizontal wavelength of roughly 1 kilometer (St. Laurent and Garrett 2002). St. Laurent and Garrett argue that it is the longer wavelengths of the internal tide which carry most of the energy flux. Thus the subcritical case is relevant to the generation of the internal tide by the large-scale topographic components of mid-ocean ridges.

The conversion rate

The main quantity of interest is the conversion rate of barotropic tidal energy into internal gravity waves. To calculate the conversion rate we begin with

the energy equation obtained from (2) and (3):

$$\tfrac{1}{2}(u^2+v^2+w^2+N^{-2}b^2)_t+\psi_x p_z-\psi_z p_x=0\,. \tag{15}$$

For the periodic flow, the average of (15) over the tidal cycle implies that

$$\nabla\cdot\boldsymbol{J}=0\,, \tag{16}$$

where $\boldsymbol{J}$ is the phase-average of the energy flux $(\psi p_z,-\psi p_x)$; using (11) this phase-averaged flux can be written as:

$$\boldsymbol{J}=\frac{\mathrm{i}U_0^2h_0^2\rho_0}{4\omega_0}\left[(N^2-\omega_0^2)(\varphi\varphi_x^*-\varphi^*\varphi_x)\,,-(\omega_0^2-f_0^2)(\varphi\varphi_z^*-\varphi^*\varphi_z)\right]\,. \tag{17}$$

The expression for $\boldsymbol{J}$ above is in the (x,z)-plane (not the (X,Z)-plane).

Above the crests of the topography the conversion is given by the integrated vertical flux of energy,

$$\mathcal{C}\equiv\frac{k_0}{2\pi}\int_{-\pi/k_0}^{\pi/k_0}\boldsymbol{J}\cdot\hat{\mathbf{z}}\,\mathrm{d}x\,. \tag{18}$$

Putting (13) and (17) into (18), we obtain $\mathcal{C}$ in terms of ϕ_n as

$$\mathcal{C}=\frac{\rho_0k_0U_0^2h_0^2}{2\omega_0}\Gamma(\epsilon) \tag{19}$$

where

$$\Gamma(\epsilon)\equiv\sum_{n=-\infty}^{\infty}|n|\phi_n(\epsilon)\phi_n^*(\epsilon)\,. \tag{20}$$

The units of $\mathcal{C}$ in (19) are Watts per square meter.

Below the crests of the topography we cannot use (18) and (19). Instead, denoting the upward topographic normal by

$$\hat{\boldsymbol{n}}\equiv(-h_x,1)/\sqrt{1+h_x^2}\,, \tag{21}$$

we can calculate $\mathcal{C}$ by integrating $\boldsymbol{J}\cdot\hat{\boldsymbol{n}}$ along the topography $z=h(x)$. This line integral following the bottom can be converted to an integral with respect to x by noting that $\mathrm{d}\ell=\mathrm{d}x\sqrt{1+h_x^2}$. We record the intermediate result that

$$\boldsymbol{J}(x,h)=-\frac{\rho_0U_0^2h_0}{2\omega_0}\varphi_{iz}(x,h)\,h\left[(N^2-\omega_0^2)h_x\,,(\,\omega_0^2-f_0^2)\right]\,. \tag{22}$$

These manipulations eventually lead to another expression for the conversion rate:

$$\mathcal{C}=-\frac{\rho_0k_0U_0^2h_0^2}{2\omega_0}\sqrt{(N^2-\omega_0^2)(\omega_0^2-f_0^2)}\int_{-\pi}^{\pi}(1-\epsilon^2H_X^2)H\varphi_{iZ}(X,\epsilon H)\,\frac{\mathrm{d}X}{2\pi}\,. \tag{23}$$

The inversion symmetry

Equation (14) has an important symmetry, obtained as follows: If we take the complex conjugate, then the left-hand side of (14), being real, does not change. But, from comparing the transformed right-hand side with that of the original equation, we conclude that

$$\phi_n(\epsilon) = \phi^*_{-n}(-\epsilon)\,. \tag{24}$$

This is *not* the well-known reality condition because ϵ has changed signs, which is equivalent to a reflection of the topography about $z = 0$ (e.g., so turning a topographic ridge into a trench). Thus, given the solution of (14) for a topographic ridge, we can use the *inversion symmetry*, (24), to obtain the solution for a trench (and vice versa).

Furthermore, using the inversion symmetry, the sum in (20) can be written as

$$\Gamma(\epsilon) = \sum_{n=1}^{\infty} n\left[\phi_n(\epsilon)\phi^*_n(\epsilon) + \phi_n(-\epsilon)\phi^*_n(-\epsilon)\right]\,. \tag{25}$$

It follows that $\Gamma(\epsilon) = \Gamma(-\epsilon)$ so that a trench and a ridge have the same conversion. This result is not intuitively obvious to us. Indeed, our proof is obscure because it relies crucially on the representation in (13). Consequently, the proof is restricted to the case of subcritical topography. In fact, when the topography is supercritical, (13) is no longer suitable because gravity waves can be radiated downwards and the resulting patterns of secondary reflections must certainly distinguish between a trench and a ridge.

3 Sinusoidal topography

In this section, we solve (14) for the sinusoidal topography $h = h_0 \cos k_0 x$. With the nondimensional coordinates of (9), the bottom is then at $Z = \epsilon H(X)$, where $H(X) = \cos X$. This sinusoidal topography has two symmetries,

$$\text{(a)}\quad H(X) = H(-X)\,, \qquad \text{(b)}\quad H(X+\pi) = -H(X)\,. \tag{26}$$

Using (26) we can make some simplifications. The first symmetry in (26a) suggests that $\phi_n = \phi_{-n}$ and consequently we can fold the sum in (14) so that $n \geq 0$. The second symmetry in (26b) indicates that θ_n defined by

$$\phi_n = \tfrac{1}{2}\mathrm{i}^{|n|-1}\theta_n\,, \tag{27}$$

is real. Taking advantage of these special sinusoidal simplifications, we bypass the general development in appendix A, and proceed directly from (14): Using the definition (27) and $\theta_n = \theta_{-n}$,

$$\cos X = -\tfrac{1}{2}\mathrm{i}\theta_0 + \sum_{n=1}^{\infty} \mathrm{i}^{n-1}\theta_n \mathrm{e}^{-\mathrm{i}n\epsilon\cos X}\cos nX\,. \tag{28}$$

Two linear systems

Invoking the Bessel function identity,

$$\mathrm{i}^n J_n(z) = \int_{-\pi}^{\pi} \mathrm{e}^{\mathrm{i}z\cos x}\cos nx\,\frac{\mathrm{d}x}{2\pi}\,, \tag{29}$$

we integrate (28) over $(-\pi, \pi)$ to obtain

$$\tfrac{1}{2}\theta_0 + \sum_{n=1}^{\infty} J_n(n\epsilon)\theta_n = 0\,. \tag{30}$$

Again we use the Bessel identity (29) to project (28) onto $\cos mX$. In this way we obtain the linear system

$$\sum_{n=1}^{\infty} \mathcal{B}_{mn}\theta_n = \delta_{1m}\,, \tag{31}$$

where the matrix elements are

$$\mathcal{B}_{mn}(\epsilon) \equiv J_{n-m}(n\epsilon) + (-1)^m J_{m+n}(n\epsilon)\,. \tag{32}$$

Notice that $\{\mathcal{B}_{mn}(0)\}$ is the identity matrix.

We began by truncating the linear system (31) and using standard techniques to solve for $\{\theta_n\}$. There were two problems with this strategy. First, as $\epsilon \to 1$, (32) becomes badly conditioned. Second, even at moderate values of ϵ, there are significant truncation errors so that the tail-end of the computed θ_n's has to be discarded.

A less obvious, but more rewarding, approach is to first rewrite (28) as

$$\cos X = -\tfrac{1}{2}\mathrm{i}\theta_0 + \tfrac{1}{2}\sum_{n=1}^{\infty} \mathrm{i}^{n-1}\theta_n \mathrm{e}^{\mathrm{i}n\xi} + \tfrac{1}{2}\sum_{n=1}^{\infty} \mathrm{i}^{n-1}\theta_n \mathrm{e}^{-\mathrm{i}n\eta}\,, \tag{33}$$

where

$$\xi \equiv X - \epsilon\cos X\,, \qquad \eta \equiv X + \epsilon\cos X\,. \tag{34}$$

Now we project (33) onto the basis set $\{\exp(\mathrm{i}m\xi)\}$. Once again, all the integrals can be evaluated analytically using (29). The key intermediate result is

$$\mathrm{i}^{m+n}\int_{-\pi}^{\pi}\mathrm{e}^{-\mathrm{i}n\eta-\mathrm{i}m\xi}\frac{\mathrm{d}\xi}{2\pi}=\frac{2n}{n-m}J_{m+n}\left[(m-n)\epsilon\right]\,. \tag{35}$$

In this fashion we find an another set of linear equations for the unknowns $\{\theta_n\}$:

$$\sum_{n=1}^{\infty}\mathcal{J}_{mn}\theta_n=2\frac{J_m(m\epsilon)}{m\epsilon}\,, \tag{36}$$

where

$$\mathcal{J}_{mn}(\epsilon)\equiv\delta_{mn}+\frac{2(-1)^m n}{n-m}J_{m+n}\left[(n-m)\epsilon\right]\,. \tag{37}$$

The advantage of (36) over (31) is that $\mathcal{J}_{mn}(\epsilon)$ is a diagonally dominant matrix even at $\epsilon=1$. Indeed, we get a useful approximate solution by taking $\mathcal{J}_{mn}(\epsilon)\approx\delta_{mn}$ in (36):

$$\theta_m(\epsilon)\approx\tilde{\theta}_m(\epsilon)\equiv 2\frac{J_m(m\epsilon)}{m\epsilon}. \tag{38}$$

Because of diagonal dominance, (36) is well-conditioned for $0<\epsilon\leq 1$ and there is no indication of truncation error. We make a comparison of the approximation (38) with numerical solutions of (36) in figure 1. We truncated the series at 200 in these numerical computations; several checks with truncations as high as 1200 showed no significant differences. Provided that $\epsilon<1$, θ_n falls exponentially with n; at $\epsilon=1$, $\theta_n\sim n^{-3/2}$ for $n\gg 1$. The detailed large-n asymptotics can be deduced from the expansion of the Bessel functions in $\tilde{\theta}_n$.

The conversion rate again

Given $\{\theta_n\}$ from (31), we calculate the conversion rate using

$$\mathcal{C}=\frac{\rho_0 U_0^2 h_0^2 k_0}{4\omega_0}\sqrt{(N^2-\omega_0^2)(\omega_0^2-f_0^2)}\;\;\Upsilon(\epsilon)\,, \tag{39}$$

where the nondimensional function $\Upsilon(\epsilon)$ obtained from (19) is

$$\Upsilon(\epsilon)\equiv\sum_{n=1}^{\infty}n\theta_n^2\,. \tag{40}$$

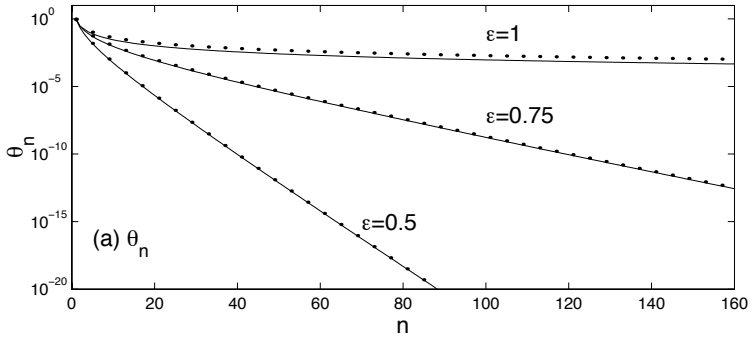

Figure 1: A comparison of the computed θ_m's with the approximation, $\tilde{\theta}_m(\epsilon)$ in (38), at $\epsilon = 0.5$, 0.75 and 1. The numerical solution of (36) is indicated by points and the approximation $\tilde{\theta}_m$ is the solid curves. The truncation of (36) used the first 200 θ_n's.

Alternatively, from (23), we have

$$\Upsilon(\epsilon) \equiv (1 - \tfrac{1}{4}\epsilon^2) \sum_{n=1}^{\infty} n\theta_n \mathcal{B}_{1n} - \tfrac{1}{4}\epsilon^2 \sum_{n=1}^{\infty} n\theta_n \mathcal{B}_{3n}\,, \tag{41}$$

where $\mathcal{B}_{mn}$ is defined in (32).

The two expressions for Υ in (40) and (41) give identical results if we have an exact solution of the linear systems in (31) and (36). Thus, we can make a nontrivial test of the accuracy of an approximate solution of (31) by computing Υ using these two different formulas and comparing the results. Figure 2 shows this comparison over the subcritical range of ϵ.

Solution using the $\epsilon \ll 1$ expansion

If ϵ is small, then we can solve (36) perturbatively and obtain the following approximations:

$$\theta_1 = 1 - \frac{\epsilon^2}{8} + \frac{3\epsilon^4}{64} + \frac{247\epsilon^6}{9216} + O(\epsilon^8)\,, \quad \theta_3 = \frac{3\epsilon^2}{8} - \frac{97\epsilon^4}{384} + O(\epsilon^6) \tag{42}$$

and

$$\theta_2 = \frac{\epsilon}{2} - \frac{5\epsilon^3}{24} + \frac{11\epsilon^5}{384} + O(\epsilon^6)\,, \quad \theta_4 = \frac{\epsilon^3}{3} + O(\epsilon^5)\,. \tag{43}$$

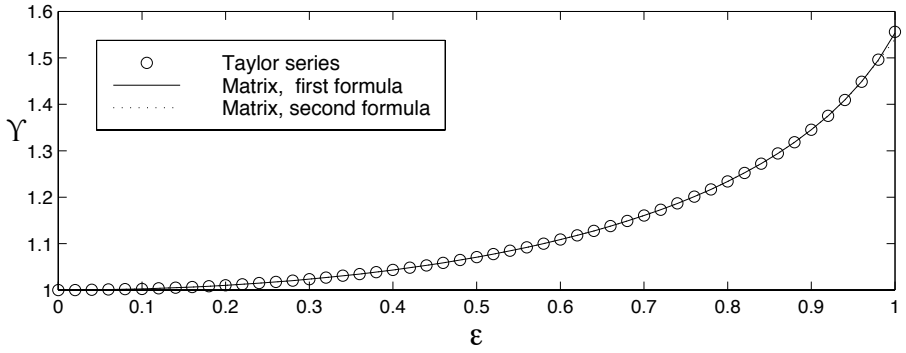

Figure 2: $\Upsilon(\epsilon)$ computed using three different methods. The Taylor series method uses 61 terms in the series (44). The first matrix formula uses the series in (40) and the second matrix formula uses the series in (41). The three methods agree to within the linewidth of the graphs. `upsilonFig.eps & sinuConvWalsh.m`

The conversion rate is then calculated from either (40) or (41):

$$\Upsilon(\epsilon) = 1 + \frac{\epsilon^2}{4} + \frac{11\epsilon^4}{96} + \frac{143\epsilon^6}{2304} + \frac{4513\epsilon^8}{122880} + \frac{170791\epsilon^{10}}{7372800} + O\left(\epsilon^{12}\right) . \quad (44)$$

The result using 61 terms in the series (44), $\Upsilon^{(61)}(\epsilon)$ (computed with the assistance of MAPLE), is shown by the open circles in figure 2. At the critical value, $\Upsilon^{(61)}(1) \approx 1.5561$.

Denoting the coefficient of ϵ^{2j} in (44) by Υ_j (e.g., $\Upsilon_1 = 1/4$) we find empirically that

$$\lim_{j\to\infty} \Upsilon_j \propto j^{-5/2} . \quad (45)$$

We conclude that the series (44) diverges if $\epsilon > 1$ and converges if $\epsilon \leq 1$. We used Padé resummation to try to extrapolate the series (44) beyond $\epsilon = 1$; the results were unsatisfactory and suggested that no solution existed in this regime. Indeed, we see below how the linear, inviscid solution diverges at $\epsilon = 1$ and fails to exist beyond.

We exploit (45) to make a more accurate estimate of $\Upsilon(1)$ using extrapolation:

$$\Upsilon_{\text{extrap}} \equiv \Upsilon^{(61)}(1) + \Upsilon_{60} \sum_{j=61}^{\infty} \left(\frac{60}{j}\right)^{5/2} \approx 1.558 . \quad (46)$$

We obtained an identical result from an extrapolation of the solutions of (36) from finite to infinite truncation using the asymptotic dependence, $\theta_n \sim n^{-3/2}$. We conclude that critical ($\epsilon = 1$) sinusoidal topography has a conversion rate that is about 56% greater than the rate calculated from weak-topography approximation ($\epsilon = 0$). This is a rather modest topographic enhancement of the dependence on h_0^2 contained in the dimensional factor on the right-hand side of (39).

Li (2002) has also calculated the conversion produced by a sinusoidal topography using a terrain-following version of the Princeton Ocean model. He finds that at $\epsilon = 1$ the conversion is greater than the weak-topography result by a factor of 1.65. The difference with our result is probably due to dissipative and discretization effects in the numerical model.

Visualization of the solution

From the computed θ_n's we rebuild the dynamical variables. To visualize the solution we use the buoyancy field:

$$b = \frac{N^2}{\mu k_0} \left[Z + \alpha(\varphi_{rX} \sin \omega_0 t - \varphi_{iX} \cos \omega_0 t) \right] , \tag{47}$$

where

$$\alpha \equiv \frac{U_0 h_0 k_0^2 \mu}{\omega_0} = \epsilon \frac{U_0 k_0}{\omega_0} . \tag{48}$$

Equation (47) shows that a necessary condition for our linearization is that $\alpha \ll 1$. Notice that $\alpha \ll 1$ is *not* equivalent to $\epsilon \ll 1$ — the factor $U_0 k_0/\omega_0$ is enough to ensure that α is small even if $\epsilon = O(1)$. Nonetheless, in order to clearly display the main features of the wave field, we take rather large values of α, such as $\alpha = 1/2$.

Figure 3 shows the wavy buoyancy field at four values of ϵ. The most striking feature of these snapshots is the development of sharply collimated beams in directions close to the critical rays for $\epsilon \to 1$ (which are at 45° in the dimensionless variables X and Z). The beams originate from the points of the topography with maximum slope, and divide the flow into square cells. Within each cell the fluid sloshes back and forth in a seiche-like fashion. At $\epsilon = 1$, the Fourier expansion of the buoyancy field has coefficients $n\theta_n \sim n^{-1/2}$; this divergent Fourier series indicates that the beams are singular. Thus, inviscid, linear theory formally breaks down at criticality. Additional physics — either nonlinearity or dissipation — is required to correctly formulate the problem for $\epsilon \geq 1$.

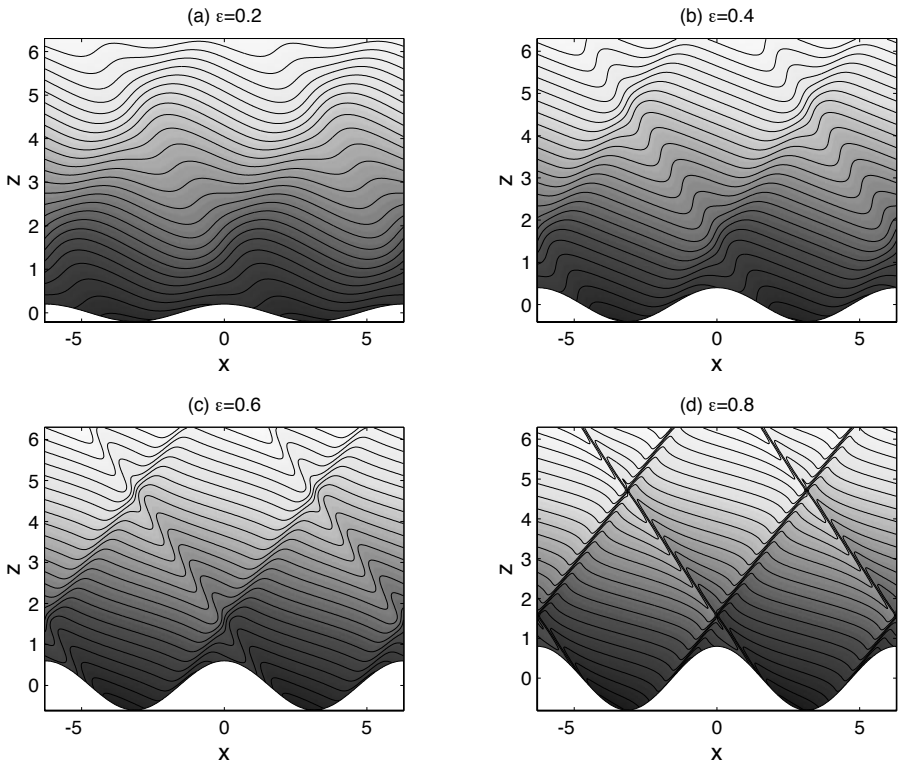

Figure 3: Snapshots of the buoyancy field computed from (47); the amplitude parameter in (48) is $\alpha = 1/2$. (a) $\epsilon = 0.2$, (b) $\epsilon = 0.4$, (c) $\epsilon = 0.6$ (d) $\epsilon = 0.8$. `wavyFig.eps, wavFigViz.m, wavFig.m`

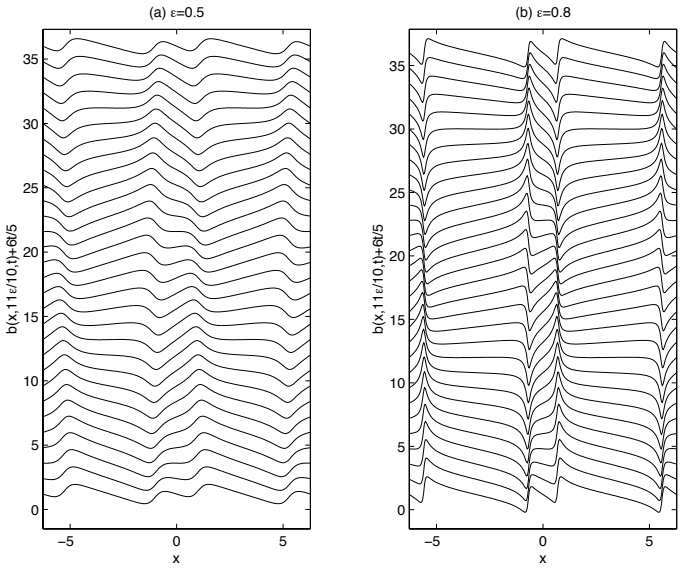

Figure 4: The sloshing buoyancy field at $Z = 1.1\epsilon$; (a) $\epsilon = 0.5$ (b) $\epsilon = 0.8$. In both panels $\alpha = 1/2$. We show a full tidal period and use an offset to separate successive snapshots.`slice1.eps`

The sloshing of the fluid within the cells is illustrated in figure 4. The curves display the buoyancy field at $z = 11\epsilon/10$ (i.e., slightly above the topographic crests at $z = \epsilon$). To show the time progression we vertically offset the curves. The very steep gradients on either side of $X = 0$ in figure 4 correspond to the beams in figure 3.

Vertical cuts through the total buoyancy field above the point of maximum topographic slope ($X = \pi/2$) are shown in figure 5. At $\epsilon = 0.5$ (panel a) there are slight overturns which become much more pronounced at $\epsilon = 0.8$ (panel b). This reversal of the vertical buoyancy gradient indicates that static instability is possible if the tide is sufficiently vigorous.

The overturning condition

Based on figure 5 we expect that for fixed ϵ there is a critical value of the amplitude parameter, α in (48), at which overturns first appear. We compute this value, say $\alpha_{\rm over}(\epsilon)$, by noticing that the maximum vertical buoyancy gradient is at $(X, Z) = (\pi/2, 0)$ and at periodically congruent points. It follows that the condition for overturning at some point in the

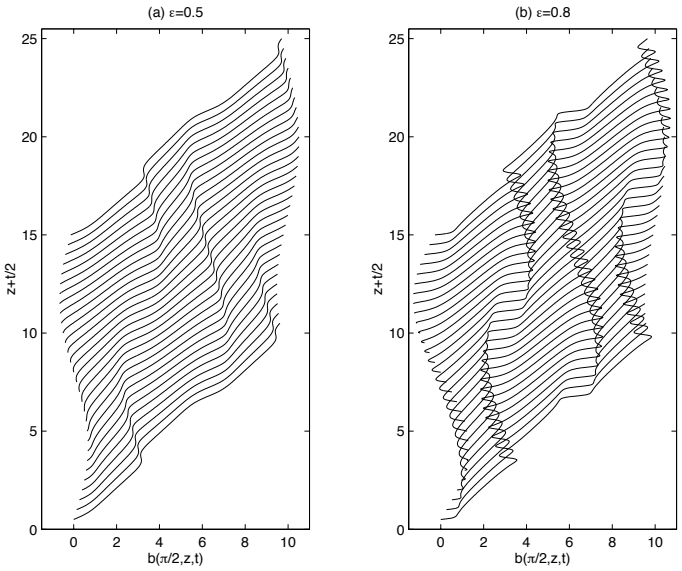

Figure 5: Buoyancy above the point of maximum slope ($X = \pi/2$); $\alpha = 1/2$. An offset is used to separate successive snapshots. Buoyancy reversals (i.e., negative values of vertical buoyancy gradient) are apparent. `overturn.eps`

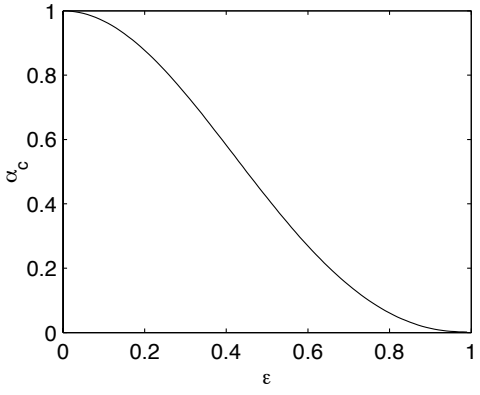

Figure 6: The function $\alpha_{\rm over}(\epsilon)$ in (49). `uvy.eps`

tidal cycle is that

$$\alpha > \alpha_{\rm over}(\epsilon) = \left[\sum_{m=0}^{\infty}(2m+1)^2\theta_{2m+1}\right]^{-1} . \tag{49}$$

Figure 6 shows $\alpha_{\rm over}(\epsilon)$. As $\epsilon \to 1$, $\alpha_{\rm over}(\epsilon) \to 0$. That is, even a very weak tide induces static instability at critical slope. This is a consequence of the singular buoyancy gradients which form all along the tidal beams in this limit.

4 An isolated bump

Now we turn to the family of topographic profiles,

$$h = h_0 \exp\left[-\gamma(1-\cos k_0 x)\right] . \tag{50}$$

If $\gamma \to 0$ we recover the sinusoidal profile of section 3 (though with $h_0 \to \gamma h_0$). On the other hand, if we write $\gamma = 1/k_0^2\ell^2$ and let $k_0 = 2\pi/\Lambda \to 0$, with ℓ fixed, then (50) is a periodically spaced sequence of well-separated Gaussian bumps; the bump at the origin is

$$h \approx h_0 {\rm e}^{-x^2/2\ell^2} . \tag{51}$$

Our main concern in this section is this limit $\gamma \to \infty$, in which we may assess the conversion of a submarine ridge by the artifice of moving the bumps further and further apart. To do this, we must demonstrate that the *total* conversion in a single wavelength, $\Lambda\mathcal{C}$, becomes independent of the bump-spacing, $\Lambda = 2\pi/k_0$, as $\Lambda \to \infty$. We provide the demonstration below.

With the profile in (50) the nondimensional parameter $\epsilon \equiv \mu h_0 k_0$ is no longer a transparent indicator of the critical slope condition. Instead, we notice that the maximum topographic slope is located at $X_m = k_0 x_m$, where

$$\cos X_m = \frac{1}{2\gamma}\left[\sqrt{1+4\gamma^2}-1\right] . \tag{52}$$

The topography becomes critical if the maximum slope is equal to the ray slope μ^{-1} defined in (8). This condition defines the critical value of ϵ:

$$\epsilon_{\rm crit}(\gamma) = \frac{{\rm e}^{\gamma(1-\cos X_m)}}{\sqrt{\gamma\cos X_m}} . \tag{53}$$

A convenient measure of the degree of criticality is then

$$\epsilon_* \equiv \epsilon/\epsilon_{\rm crit} , \tag{54}$$

so that the topographic slope is critical at $\epsilon_* = 1$.

The weak topography limit

If ϵ_* is sufficiently small (that is, 'weak' topography) we solve (14) by neglecting the term $-|n|\mu h(x)$ in the exponential on the right-hand side. In this case (14) is a Fourier series and we obtain:

$$\phi_n^{\text{weak}} = \mathrm{e}^{-\gamma} I_n(\gamma)\,, \tag{55}$$

where I_n is the modified Bessel function. The right hand side of (55) is the n'th coefficient in the Fourier series expansion of the nondimensional topography $H(X) = \exp\left[-\gamma(1-\cos X)\right]$.

The conversion rate follows from (19):

$$\mathcal{C}_{\text{weak}} = \frac{\rho_0 U_0^2 h_0^2 k_0}{4\pi\omega_0}\sqrt{(N^2-\omega_0^2)(\omega_0^2-f_0^2)}\,\Xi(\gamma)\,, \tag{56}$$

where

$$\Xi(\gamma) \equiv 4\pi \mathrm{e}^{-2\gamma}\sum_{n=1}^{\infty} n I_n^2(\gamma)\,. \tag{57}$$

The function $\Xi(\gamma)$ is shown in figure 7.

The formula (56) is equivalent to the results given by Bell (1975a) and Llewellyn Smith and Young (2002). Indeed, we notice that

$$\lim_{k_0\to\infty}\frac{2\pi}{k_0}\mathcal{C}_{\text{weak}} = \frac{\rho_0 U_0^2 h_0^2}{2\omega_0}\sqrt{(N^2-\omega_0^2)(\omega_0^2-f_0^2)}\,. \tag{58}$$

The result above agrees with the conversion rate of a single, weak Gaussian bump given by Llewellyn Smith and Young (2002).

Finite amplitude topography

If ϵ_* is not small then we solve (14) numerically by again forming sets of linear equations. The profiles still possess the symmetry in (26a) so that we fold the sum as in (28). We obtain a system analogous to (36), save that the matrix elements must be obtained by quadrature, and the θ_n's are no longer real. Figure 8 shows the computed internal tide above well-separated Gaussian bumps. Again the wave-field is characterized by sharply collimated beams. Partly as a result, there is almost no wave activity between the bumps. Thus we argue that solutions in figure 8 provide reliable estimates of the conversions produced by isolated topographic features.

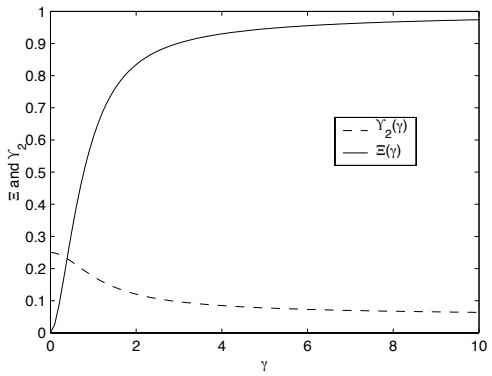

Figure 7: The solid curve is the function $\Xi(\gamma) \equiv 4\pi \sum_{n=1}^{\infty} n I_n^2(\gamma)$ in (56) and (57). The dashed curve is the function $\Upsilon_2(\gamma)$ defined in the discussion surrounding (60). `nog.eps`

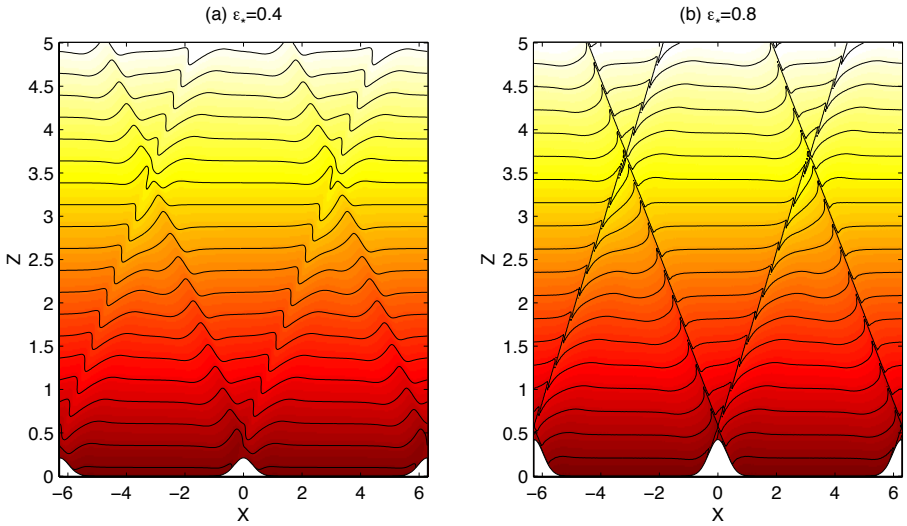

Figure 8: Snapshots of the buoyancy field above well separated bumps; $\gamma = 10$ and $\alpha = 1/5$. Panel (a) shows $\epsilon_* = 0.4$ and panel (b) $\epsilon_* = 0.8$. `burshot1.eps`

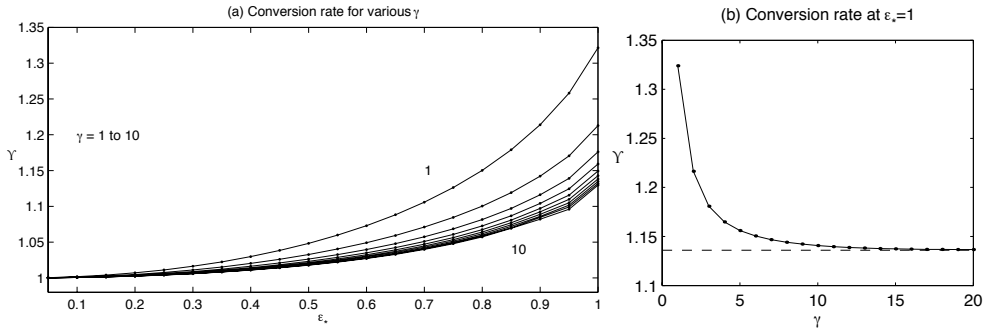

Figure 9: Left panel: $\Upsilon(\epsilon_*, \gamma)$ in (59) with $\gamma = 1,\ 2\ ....\ 10$ and $0 < \epsilon_* < 1$. At fixed ϵ_* the conversion rate decreases as we approach the isolated-bump limit by increasing γ. The left panel shows $\Upsilon(1, \gamma)$; if γ is greater than about 10, $\Upsilon(1, \gamma)$ is independent of γ. `newbully.eps, newbully2.eps`

We write the conversion rate for finite slopes in the form,

$$\mathcal{C} = \mathcal{C}_{\rm weak} \Upsilon(\epsilon_*, \gamma)\,, \tag{59}$$

where $\Upsilon(0, \gamma) = 1$ and $\mathcal{C}_{\rm weak}$ is defined in (56). The nondimensional function Υ measures the degree to which the conversion rate is enhanced above the weak-topography estimate in (56). Figure 9 shows the computed function $\Upsilon(\epsilon_*, \gamma)$.

Once γ is greater than about 10 the results in figure 9 are independent of γ. That is, there is no interference between adjacent Gaussian bumps. At $\epsilon_* = 1$ we estimated the limit $\gamma \to \infty$ using extrapolation and found that $\Upsilon(1, \infty) \approx 1.136$. In other words, at critical slope, the conversion of an isolated Gaussian bump is only 14% greater than the weak-topography estimate.

We also computed the second-order terms in the expansion of the enhancement factor, $\Upsilon(\epsilon_*, \gamma)$ in (59), using the method of Appendix B. We find that

$$\Upsilon(\epsilon_*, \gamma) = 1 + \Upsilon_2(\gamma)\epsilon_*^2 + O(\epsilon_*^4)\,, \tag{60}$$

where $\Upsilon_2(\gamma)$ is evaluated by summing a Bessel series (see figure 7). In agreement with the sinusoidal limit in (44) we recover $\Upsilon_2(0) = 1/4$. As an indication of the asymptotic value for an isolated Gaussian we find $\Upsilon_2(100) = 0.0515$.

The results of Baines (1972) are the only previous calculations for ridge-like topography which are in the same $\epsilon_* = O(1)$ parameter range as those in figure 9. It is difficult to make a useful comparison because Baines does not factor out the dependence of the conversion on the factor h_0^2 contained in $\mathcal{C}_{\rm weak}$ – see (56) and (59). Thus figure 6 of Baines shows mainly $\mathcal{C} \propto h_0^2$; without normalization by $\mathcal{C}_{\rm weak}$ it is impossible to detect the small corrections to $\mathcal{C}_{\rm weak}$ contained in Υ.

5 Fourier superposition and random topography

The main result of the previous sections is that the enhancement factor, Υ, increases monotonically and modestly with ϵ. Moreover, for the sinusoid, the first effect of $\epsilon \neq 0$ is the quadratic term, $\epsilon^2/4$, on the right hand side of (44). The corresponding result for the Gaussian ridge is the term $\Upsilon_2(\infty) \approx 0.0515$ in (60). These simple results seem to depend crucially on the form of the topography. In the remainder of this paper we assess tidal conversion by topographic profiles that more closely represent the rough ocean floor.

Random topography

We consider an ensemble of topographies, $h = h_0 H^\chi(X)$, where $H^\chi(X)$ denotes a realization (labelled by χ) of the profile constructed by randomly selecting the complex coefficients, $H_n^\chi = H_n^{(\chi r)} + {\rm i} H_n^{(\chi i)}$, of the Fourier representation,

$$H^\chi(X) = \sum_{-n_c}^{n_c} H_n^\chi {\rm e}^{{\rm i}nX} \,; \tag{61}$$

n_c is a spectral cut-off. We take $H_n^{(\chi r)}$ and $H_n^{(\chi i)}$ to be independent and normally distributed random variables with a Gaussian probability density function. In other words, if $n > 0$, we pick $H_n^{(\chi r)}$ and $H_n^{(\chi i)}$ from the density

$$\mathcal{P}\left(H_n^{(\chi r)}\right) = \frac{1}{\sqrt{2\pi\sigma_n^2}} \exp\left(-{H_n^{(\chi r)}}^2/2\sigma_n^2\right) . \tag{62}$$

We obtain the $n < 0$ coefficients from the reality condition, $H_n^\chi = H_{-n}^{\chi *}$. With this recipe, the RMS topographic height is given by

$$h_{\rm RMS}^2 = \sum_{n=1}^{n_c} \mathcal{S}(n) \,, \tag{63}$$

where $\mathcal{S}(n) \equiv 4h_0^2\sigma_n^2$ is a discrete form of the power spectral density.

In the weak-topography limit, one takes $\phi_n^\chi = H_n^\chi$ and calculates the conversion using (19)-(20). This allows a certain degree of headway in analysing the effect of different choices for the σ_n's and n_c. But once ϵ is nonzero, this analytic avenue is no longer open. Instead, we rely on a combination of numerical computation and a small-ϵ expansion analogous to (44).

For illustration, we use model topographic spectrum suggested by Bell (1975b) and Goff & Jordan (1988):

$$\mathcal{S}(n) \equiv 4h_0^2\sigma_n^2 = 4h_0^2 \begin{cases} \left[n_*^2 + n^2\right]^{-q/2} , & \text{if } n \le n_c, \\ 0 , & \text{if } n > n_c . \end{cases} \tag{64}$$

The model spectrum (64) has four parameters: n_c, h_0, n_* and the exponent q. According to Bell (1975b) and Goff & Jordan (1988), submarine topography is characterized by a spectral exponent in the range $2 < q < 3$. We use the specific parameter settings,

$$n_* = 4 , \quad n_c = 32 , \quad q = 5/2 . \tag{65}$$

We continue to use the definition $\epsilon \equiv h_0 k_0 \mu$. But, again, the critical value of ϵ is no longer unity. Instead, each realization of the topography has a different maximum slope, say $s_{\max}^\chi$. Thus we introduce a rescaled parameter, defined as

$$\epsilon_*^\chi \equiv \epsilon s_{\max}^\chi . \tag{66}$$

With this definition, a particular realization of the topography has a critical slope when $\epsilon_*^\chi = 1$.

A few realizations

We solve (14) for ϕ_n using the method outlined in appendix A. Typical results are shown in figures 10-12. With $n_c = 32$, the topography is a random superposition of 32 sinusoids. But in order to reliably represent the wavefield over the range $0 < \epsilon_* \le 0.95$, we retained 256 sinusoids in (13). The upper panel of figure 10 shows a sample topographic profile. The lower panel of figure 10 displays the corresponding periodogram of the topography (nonzero only if $1 < n < 32$), together with the computed coefficients, ϕ_n, of the wavefield at $\epsilon = 0.03$ (nonzero if $1 < n < 256$). Figure 11 shows the wavy buoyancy field above random topography of figure 10 with a particular choice for the tidal amplitude ($\alpha = 0.01$ in (48)).

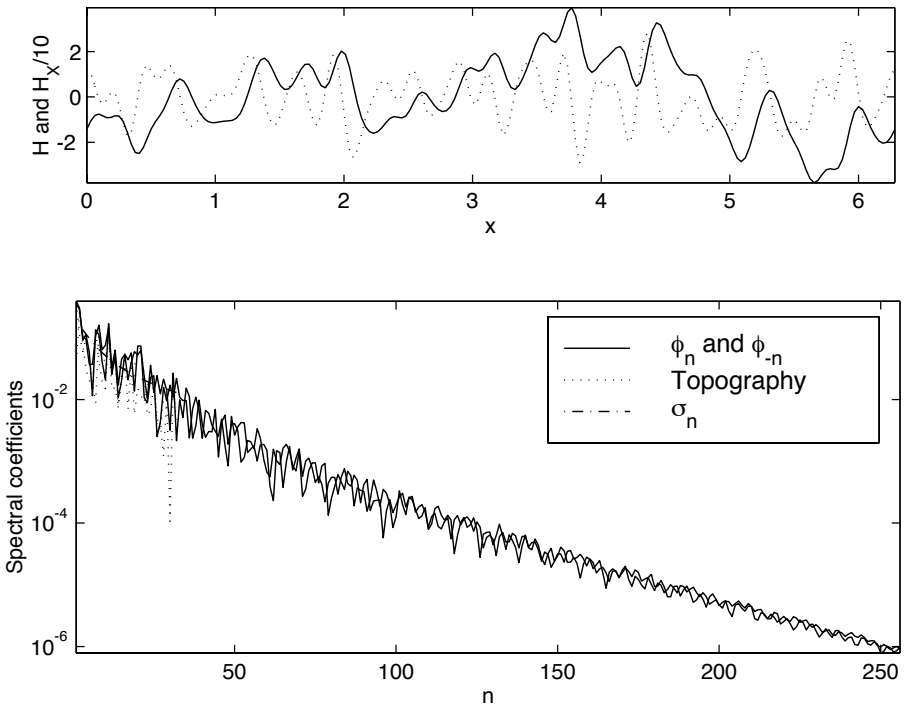

Figure 10: An example of a topographic profile constructed according to (61) through (65). The upper panel shows $H(X)$ (the solid curve) and $H_X/10$ (the dotted curve). The lower panel shows the spectral coefficients of the topography and of the solution of (14). The topographic periodiogram is limited to $1 < n \leq n_c = 32$. In this illustration $\epsilon = 0.03$, $\epsilon_* = 0.44$. `randy1.eps`

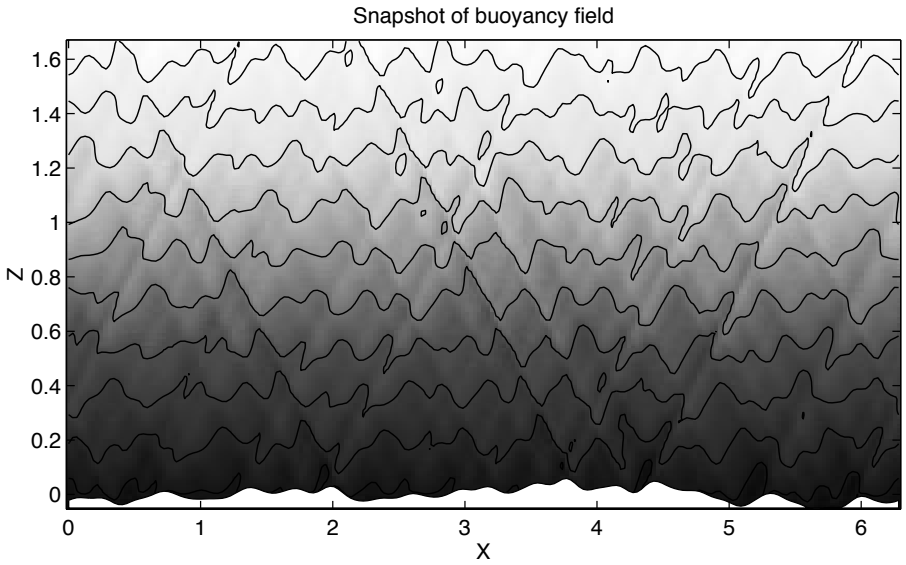

Figure 11: An example of the wave field above a realization of the random topography. In this illustration $\epsilon = 0.03$, $\epsilon_* = 0.44$ and the amplitude in (48) is $\alpha = 0.01$. The most striking features in the wavefield are the beams emanating from the steepest slopes of the topography `.randy2.eps`

According to (19) and (20), the conversion is proportional to the sum,

$$\Gamma(\epsilon,\chi) \equiv \sum_{n=-\infty}^{\infty} |n||\phi_n^\chi(\epsilon)|^2 \,. \tag{67}$$

Figure 12 summarizes the conversion generated over fourteen different realizations. The dashed curves in the left-hand panel show the functions $\Gamma(\epsilon,\chi)$ with $\chi = 1,\ldots,14$. It is striking that the variations in conversion between different realizations are much greater than the slight enhancements which result from increasing ϵ_*^χ from 0 to 0.95. In the right-hand panel of figure 12 we show the enhancement factor,

$$\Upsilon(\epsilon,\chi) \equiv \Gamma(\epsilon,\chi)/\Gamma(0,\chi), \tag{68}$$

plotted against the rescaled parameter ϵ_*^χ defined in (66). At $\epsilon_*^\chi = 0.95$ — the largest value we could reliably compute with 256 sinusoids in the wavefield — the enhancement is only about 4 to 8% greater than the weak topography result, obtained by putting $\phi_n^\chi \approx H_n^\chi$ in (67).

The ensemble-averaged conversion rate to second order in ϵ

With the spectral formulation, we can compute ensemble averages of the conversion rate by Monte Carlo simulation. The average conversion rate, estimated for 10^4 realizations over the range $0 < \epsilon < 0.01$, is well fit by the relation,

$$\begin{aligned}\langle \mathcal{C} \rangle = &\frac{\rho_0 U_0^2}{2\omega_0}\sqrt{(N^2-\omega_0^2)(\omega_0^2-f_0^2)}k_0 \\ &\times \langle \Gamma(0)\rangle \left[1+\epsilon^2\Upsilon_2 + O(\epsilon^4)\right] \,,\end{aligned} \tag{69}$$

with $\langle\Gamma(0)\rangle \approx 2.5912$ and $\Upsilon_2 \approx 12.316$. These numbers can be predicted analytically (and more usefully) using perturbation theory for small ϵ.

The perturbation expansion is described in detail in Appendix B; briefly, we expand (14) and compute the solution for ϕ_n by iteration to order ϵ^2. We then insert the result into the formula for the conversion rate, ensemble average using the probability density functions in (62), and find

$$\begin{aligned}\langle \mathcal{C} \rangle = &\frac{\rho_0 U_0^2}{2\omega_0}\sqrt{(N^2-\omega_0^2)(\omega_0^2-f_0^2)}k_0 \\ &\times \left[\sum_{n=1}^{\infty} n\mathcal{S}(n) + \frac{\mu^2 k_0^2}{4}\sum_{m=1}^{\infty}\sum_{n=1}^{\infty} A(m,n)\mathcal{S}(m)\mathcal{S}(n) + O(\mu^4\mathcal{S}^3)\right] \,,\end{aligned} \tag{70}$$

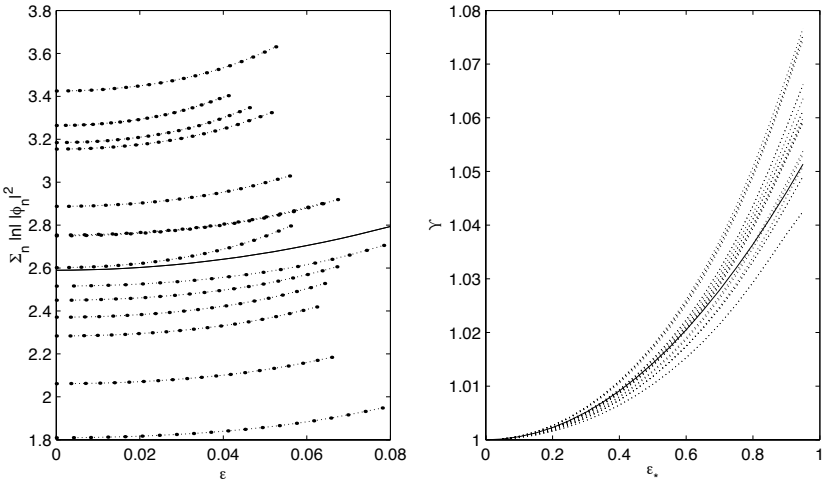

Figure 12: Left panel: the 14 dashed curves show the sum $\Gamma(\epsilon)$ in (67) calculated using 14 realizations of the topography. The maximum slope, $s^{\chi}_{\max}$, was typically of order 15 and so $\epsilon_* = 0.95$ corresponds to maximum values of ϵ of about 0.06. The right panel shows the enhancement factor for the fourteen topographies, $\Upsilon(\chi, \epsilon^{\chi}_*) \equiv \Gamma(\epsilon, \chi)/\Gamma(0, \chi)$. In this right panel we use the rescaled parameter ϵ^{χ}_* defined in (66) as the abscissa. In both panels, the solid curve shows the results expected from the small-ϵ perturbation theory. `runplot.eps`

where $A(m,n) \equiv (m+n)(m^2+n^2-|m^2-n^2|)$. Bell's (1975b) result is the first term in the square bracket on the right hand side of (70), and expresses the conversion rate, averaged over the topographic ensemble, in terms of the topographic power spectral density. Our second-order correction is the final double sum. For the parameter values in (65), one finds the result in (69) with the same value for $\langle\Gamma(0)\rangle$, and $\Upsilon_2 \approx 12.3152$.

The prediction $2.5912(1+12.3152\epsilon^2)$ from (70) is shown as the solid curve in the left-hand panel of figure 12. In order to display this same prediction in the right-hand panel, we must convert ϵ to an "average ϵ_*". To do this, we computed the average of the maximum slopes using our ensemble of $10,000$ topographic profiles; we found that $\langle s_{\max}\rangle \approx 14.7$. Thus we define

$$\langle\epsilon_*\rangle = 14.7\epsilon\,. \tag{71}$$

so that the prediction in (69) is

$$\Upsilon(\langle\epsilon_*\rangle) = 1 + 0.057\langle\epsilon_*\rangle^2\,. \tag{72}$$

The parabola in (72) is the solid curve in the right-hand panel of figure 12.

6 Conclusions and discussion

Our focus in this work has been the conversion rate of energy from the barotropic tide into internal gravity waves at topography with finite slope. The results indicate that Bell's weak-topography approximation provides reliable estimates of this conversion. For example, we have shown that for an isolated Gaussian ridge the conversion rate at critical slope is only 14% greater than the weak-slope result obtained by Llewellyn Smith and Young (2002) using Bell's approach. In the case of random topographies, having a power spectral density with a slope of -2.5, there are factor-of-two fluctuations in conversion rate between different topographic realizations. These sample fluctuations are much greater than the 4 to 8% enhancement above the weak-topography estimate occurring as the amplitude of a single realization is increased (see figure 12). This result suggests that the major uncertainty in estimating ocean conversion rates is adequate knowledge of ocean topography.

St. Laurent & Garrett (2002) have argued that, because the Richardson number of the internal tide is large, vigorous shear instability will not typically occur. Thus, even given significant energy conversion, there are still important questions surrounding the degradation of the internal tide into

small-scale mixing (see also Polzin 2002). Our visualizations of the radiated wave-field show sharply collimated beams leaving the point of maximum topographic slope; density overturns and mixing might occur in these beams. Indeed, as the critical slope is approached, even a very weak barotropic tide is sufficient to produce overturns at some phase of the tidal cycle (see figure 6). In other words, while increasing ϵ_* does not greatly enhance the conversion rate, steeper topographic slopes do produce smaller spatial scales in the radiated waves. Thus, a key effect of large topography may be to destabilize the internal tide through the formation of the small-scale features evident in our visualizations of the wave field.

At $\epsilon_* = 1$, our solutions become singular via the appearance of diverging buoyancy gradients. This signifies a breakdown of inviscid, linear theory. It seems that useful results for the supercritical case must consider the physical processes (nonlinearity and viscosity) which heal the singularity that attends the transition at $\epsilon_* = 1$. Nevertheless, in all the cases we studied, there is no indication of dramatic changes in the conversion rate at the critical point $\epsilon_* = 1$. Moreover, the numerical results of Li (2002) and Khatiwala (2002) suggest that conversion above supercritical topography either saturates or begins to decline with increasing ϵ_*. If these results are reliable indications of what happens in the supercritical regime, then the weak topography approximation is very useful tool over the entire range of ϵ_*.

Acknowledgements

WRY is supported by NSF OCE96-16017. NJB was partly supported by a faculty research grant from UCSC. A substantial portion of this work was completed at the 2001 WHOI GFD program, which is supported by NSF and ONR; we thank Joe Keller and Chris Garrett for discussions.

A Reduction of equation (14) to a linear system

We rewrite (14) in the form

$$H(X) = \phi_0 + \sum_{m=1}^{\infty} \phi_m \exp\left[\mathrm{i}m\xi\right] + \sum_{m=1}^{\infty} \hat{\phi}_m \exp\left[-\mathrm{i}m\eta\right] , \tag{73}$$

where $\hat{\phi}_m \equiv \phi_{-m}$ and

$$\xi \equiv X - \epsilon H(X) , \qquad \eta \equiv X + \epsilon H(X) . \tag{74}$$

Guided by the experience gained from studying sinusoidal topography, we project (73) on $\exp(-\mathrm{i}n\xi)$ and $\exp(\mathrm{i}n\eta)$, to obtain the linear system,

$$\sum_{m=1}^{\infty} \mathcal{A}_{nm}\hat{\phi}_m + \phi_n = \varpi_n\,,$$
$$\sum_{m=1}^{\infty} \hat{\mathcal{A}}_{nm}\phi_m + \hat{\phi}_n = \hat{\varpi}_n\,. \tag{75}$$

In (75)

$$\varpi_n(\epsilon) \equiv \oint \mathrm{e}^{-\mathrm{i}n\xi} H(X)\frac{\mathrm{d}\xi}{2\pi}$$
$$= \frac{1}{\mathrm{i}n\epsilon}\oint \mathrm{e}^{-\mathrm{i}n\xi}\frac{\mathrm{d}X}{2\pi}\,, \tag{76}$$

and $\hat{\varpi}_n(\epsilon) = \varpi_n^*(-\epsilon)$. In (76), $\oint$ indicates an integral over a period, say from $X = -\pi$ to π.

The matrices in (75) are

$$\mathcal{A}_{nm}(\epsilon) = \oint \mathrm{e}^{-\mathrm{i}n\xi - \mathrm{i}m\eta}\,\frac{\mathrm{d}\xi}{2\pi}\,,$$
$$\hat{\mathcal{A}}_{nm}(\epsilon) = \oint \mathrm{e}^{\mathrm{i}n\eta + \mathrm{i}m\xi}\,\frac{\mathrm{d}\eta}{2\pi}\,. \tag{77}$$

The diagonal elements of these matrices can be further simplified to

$$\left[\mathcal{A}_{mm}, \hat{\mathcal{A}}_{mm}\right] = -2\mathrm{i}m\epsilon\,[H_{2m}, H_{2m}^*]\,, \tag{78}$$

where H_p is the coefficient of $\exp(\mathrm{i}pX)$ in the Fourier series representation of $H(X)$ (e.g., as in (61)). The off-diagonal terms of $\mathcal{A}_{nm}$ and $\hat{\mathcal{A}}_{nm}$ can be expressed concisely in terms of the matrix,

$$\mathcal{K}_{nm}(\epsilon) = \oint \mathrm{e}^{-\mathrm{i}(m+n)X + \mathrm{i}(n-m)\epsilon H(X)}\frac{\mathrm{d}X}{2\pi}\,. \tag{79}$$

We find that

$$\mathcal{A}_{nm}(\epsilon) = \frac{2m}{m-n}\mathcal{K}_{nm}(\epsilon)\,, \quad (m \neq n)\,, \tag{80}$$

and

$$\hat{\mathcal{A}}_{nm}(\epsilon) = \frac{2m}{m-n}\mathcal{K}_{nm}^*(-\epsilon) = \frac{2m}{m-n}\mathcal{K}_{mn}^*(\epsilon) = -\frac{m}{n}\mathcal{A}_{mn}^*(\epsilon)\,. \tag{81}$$

For the calculations in section **5** we numerically computed ϖ_n and $\mathcal{A}_{mn}$ from (76), (79) and (80) using X (rather than ξ) as the variable of integration. Equation (81) then enables one to efficiently obtain the matrix $\hat{\mathcal{A}}(\epsilon)$ from the transpose-conjugate of $\mathcal{A}(\epsilon)$.

The system (75) can be reduced to:

$$\phi_n - \sum_{m=1}^{\infty}\sum_{p=1}^{\infty}\mathcal{A}_{nm}\hat{\mathcal{A}}_{mp}\phi_p = \varpi_n - \mathcal{A}_{nm}\hat{\varpi}_m \tag{82}$$

by eliminating the hatted variables. After truncating and solving (82) for ϕ_n one can then directly obtain $\hat{\phi}_n$ from the second equation in (75).

B The second-order correction

This appendix summarizes the calculations leading to the second-order correction to Bell's formula in (70). We begin by expanding (14) in powers of ϵ:

$$H(X) = \sum_n \phi_n e^{inX} e^{-i|n|\epsilon H(X)} = \sum_n \phi_n e^{inX}\left[1 - i|n|\epsilon H - \frac{1}{2}n^2\epsilon^2 H^2 + ...\right] \tag{83}$$

We solve this equation iteratively

$$\begin{aligned}\phi_n =& H_n + i\epsilon\sum_p |n-p|H_pH_{n-p} \\ &+ \frac{1}{2}\epsilon^2\sum_{p,q}[(n-p-q)^2 - 2|(n-p-q)(n-q)|]H_pH_qH_{n-p-q}\,.\end{aligned} \tag{84}$$

Substituting into (20) we find

$$\begin{aligned}\Gamma =& \sum_n |n||H_n|^2 + i\epsilon\sum_{n,p}|n(n-p)|[H_pH_{n-p}H_n^* - H_p^*H_{n-p}^*H_n] \\ &+ \epsilon^2\sum_{n,p,q}|n(n-p)(n-q)|H_pH_q^*H_{n-p}H_{n-q}^* \\ &+ \frac{\epsilon^2}{2}\sum_{n,p,q}|n+p+q|[n^2 - 2|n(n+p)|](H_pH_qH_nH_{n+p+q}^* + H_p^*H_q^*H_n^*H_{n+p+q})\,.\end{aligned} \tag{85}$$

We ensemble average:

$$\Big\langle \sum_n |n||H_n|^2 \Big\rangle = 4 \sum_{n>0} n\sigma_n^2 \,. \tag{86}$$

The $O(\epsilon)$ term in Γ is uncorrelated and vanishes. The hard part is the fourth-order correlation: To compute this, we evaluate two terms separately. First, we have $\langle H_p H_q^* H_{n-p} H_{n-q}^* \rangle$. In order for the correlation not to vanish, the average must break up into either a true fourth-order correlation (in which all the H_j's have the same index, modulo sign), or two independent pairs (second-order correlations, with paired indices). The true fourth-order correlation arises for $p = \pm q$, $p = \pm(n-p)$, and $p = \pm(n-q)$. These conditions are consistent only if $2p = 2q = n$, bearing in mind that $n = 0$ is not allowed. The possible paired second-order correlations are

$$\begin{Bmatrix} p = \pm q \\ n-p = \pm(n-q) \end{Bmatrix}, \qquad \begin{Bmatrix} p = \pm(n-p) \\ q = \pm(n-q) \end{Bmatrix}, \qquad \text{and} \qquad \begin{Bmatrix} p = \pm(n-q) \\ q = \pm(n-p) \end{Bmatrix}. \tag{87}$$

Again, we exclude many of these possibilities by demanding consistency and by arguing that p, q and n cannot vanish. Only $p = q$ and $n = p + q$ give independent pairs. Thus,

$$\begin{aligned} \langle H_p H_q^* H_{n-p} H_{n-q}^* \rangle =& \langle |H_p|^2 \rangle \langle |H_{n-p}|^2 \rangle \delta_{p,q} + \langle |H_p|^2 \rangle \langle |H_q|^2 \rangle \delta_{n,p+q} \\ &+ \langle |H_p|^4 \rangle \delta_{p,q} \delta_{2p,n} - 2 \langle |H_p|^2 \rangle^2 \delta_{p,q} \delta_{2p,n} \,, \end{aligned} \tag{88}$$

where the final term represents the twice overcounted fourth-order correlation which not should not appear as either of the independent pairings. This contribution to $\langle \Gamma \rangle$ can then be written in the form,

$$2 \sum_{p,q} |p+q| (|q| + |p|)^2 \sigma_p^2 \sigma_q^2, \tag{89}$$

given that $\langle |H_p|^4 \rangle = 8\sigma_p^4$.

A similar computation provides the other fourth-order term:

$$\begin{aligned} \langle H_p H_q H_n H_{n+p+q}^* \rangle =& \langle |H_p|^2 \rangle \langle |H_n|^2 \rangle \delta_{p,-q} \\ &+ \langle |H_p|^2 \rangle \langle |H_q|^2 \rangle \delta_{p,-n} + \langle |H_p|^2 \rangle \langle |H_q|^2 \rangle \delta_{q,-n} \\ &+ (\langle |H_p|^4 \rangle - 2 \langle |H_p|^2 \rangle^2)(\delta_{p,-q}\delta_{p,n} + \delta_{p,-q}\delta_{p,-n} + \delta_{p,-n}\delta_{p,q}) \,. \end{aligned} \tag{90}$$

(the illegal pairs are for $p = \pm n$ in the first term, $p = \pm q$ in the second, and $p = \pm q$ in the third, which leads to the subtracted term). The associated contribution to Γ is

$$2\sum_{p,q}[|q|^3 + |p|^3 + 2|pq|(|p| + |q|) - 2|p + q|(|p| + |q|)^2]\sigma_p^2\sigma_q^2 \qquad (91)$$

The $O(\epsilon^2)$ term is therefore

$$4\sum_{p,q>0}(p + q)[q^2 + p^2 - |p^2 - q^2|]\sigma_p^2\sigma_q^2. \qquad (92)$$

Hence,

$$\Gamma = \sum_{n>0} 4n\sigma_n^2 + \epsilon^2 \sum_{p,q>0} 4(p + q)[q^2 + p^2 - |p^2 - q^2|]\sigma_p^2\sigma_q^2\,. \qquad (93)$$

Using $\mathcal{S}(n) = 4h_0^2\sigma_n^2$ to eliminate σ_n^2, and substituting Γ into (19), we obtain the expression for the ensemble-averaged conversion to $O(\epsilon^2)$ given in (70).

References

[1] P. G. Baines, 1973. The generation of internal tides by flat-bump topography. *Deep-Sea Res.,* **20,** 179-205.

[2] T.H. Bell, 1975(a). Lee waves in stratified fluid with simple harmonic time dependence. *J. Fluid Mech.,* **67,**705-722.

[3] T.H. Bell, 1975(b). Topographically generated internal waves in the open ocean. *J. Geophys. Res.* **80,** 320-327.

[4] J.A. Goff and T. H. Jordan, 1988. Stochastic modelling of seafloor morphology: inversion of sea beam data and second-order statistics. *J. Geophys. Res.* **93** B11, 13,598-13,608.

[5] P.E. Holloway and M.A. Merrifield, 1999. Internal tide generation by seamounts, ridges and islands. *J. Geophys. Res.,* **104,** C11, 25,937-25,951.

[6] S. Khatiwala, 2002. Generation of internal tides in the Ocean. Submitted to *Deep-Sea Research.*

[7] J.B. Keller, 2000. Singularities and Rayleigh's hypothesis for diffraction gratings. *J. Opt. Soc. Am. A* **17**, 456-457.

[8] J.R. Ledwell, E.T. Montgomery, K.L. Polzin, L.C. St. Laurent, R.W. Schmitt and J.M. Toole, 2000. Evidence of enhanced mixing over rough topography in the abyssal ocean. *Nature,* **403,** 179-182.

[9] S.G. Llewellyn Smith and W.R. Young, 2002. Conversion of the barotropic tide. In press in the *J. Phys. Oceanogr.*

[10] M. Li, 2002. Energetics of internal tides radiated from deep-ocean topographic features Submitted to *J. Mar. Res.*

[11] W.H. Munk and C.I. Wunsch 1998. Abyssal recipes II: energetics of tidal and wind mixing. *Deep-Sea Res.,* **45**, 1977-2010.

[12] K.L. Polzin 2002. Idealized solutions for the energy balance of the finescale internal wavefield. Submitted to *J. Mar. Res.*

[13] L. St. Laurent and C. Garrett, 2002. The role of internal tides in mixing the deep ocean. Submitted to *J. Physical Oceanogr.*